Nanoscale

PAPER

View Article Online
View Journal | View Issue

Cite this: *Nanoscale*, 2018, **10**, 1196

One-step coelectrodeposition-assisted layer-by-layer assembly of gold nanoparticles and reduced graphene oxide and its self-healing three-dimensional nanohybrid for an ultrasensitive DNA sensor†

Jayakumar Kumarasamy, [a,c,e] María Belén Camarada, [b] Dharuman Venkatraman,*[a] Huangxian Ju, [c] Ramendra Sundar Dey*[d] and Yangping Wen *[e]

A layer-by-layer (LBL) assembly was employed for preparing multilayer thin films with a controlled architecture and composition. In this study, we report the one-step coelectrodeposition-assisted LBL assembly of both gold nanoparticles (AuNPs) and reduced graphene oxide (rGO) on the surface of a glassy carbon electrode (GCE) for the ultrasensitive electrochemical impedance sensing of DNA hybridization. A self-healable nanohybrid thin film with a three-dimensional (3D) alternate-layered nanoarchitecture was obtained by the one-step simultaneous electro-reduction of both graphene oxide and gold chloride in a high acidic medium of H_2SO_4 using cyclic voltammetry and was confirmed by different characterization techniques. The DNA bioelectrode was prepared by immobilizing the capture DNA onto the surface of the as-obtained self-healable AuNP/rGO/AuNP/GCE with a 3D LBL nanoarchitecture *via* gold–thiol interactions, which then served as an impedance sensing platform for the label-free ultrasensitive electrochemical detection of DNA hybridization over a wide range from 1.0×10^{-9} to 1.0×10^{-13} g ml^{-1}, a low limit of detection of 3.9×10^{-14} g ml^{-1} (S/N = 3), ultrahigh sensitivity, and excellent selectivity. This study presents a promising electrochemical sensing platform for the label-free ultrasensitive detection of DNA hybridization with potential application in cancer diagnostics and the preparation of a self-healable nanohybrid thin film with a 3D alternate-layered nanoarchitecture *via* a one-step coelectrodeposition-assisted LBL assembly.

Received 18th September 2017,
Accepted 1st December 2017

DOI: 10.1039/c7nr06952a

rsc.li/nanoscale

1. Introduction

DNA sensors have been intensively employed for infection diseases assays, pathogens recognition, cancer diagnosis, environmental monitoring, and other purposes. Electrochemical devices are very easy to miniaturize, intelligentize, modularize, integrate, and multi-functionalize. Moreover, electrochemical transducers are reasonably simple, rapid, and inexpensive, and the electrochemical transduction is independent of solution turbidity or the optical pathway. They have been widely utilized for highly sensitive determination of DNA hybridization. Almost all electrochemical DNA sensors are based on the use of commercially available substrate electrodes obtained by sealing metal or carbon materials into plastic supports. Recently, substrate electrodes assembled/modified by various nanomaterials as promising sensing platforms have been explored/exploited for the amplified detection of DNA to overcome safety problems, poor sensitivity, and bad stability.[1,2]

The immobilization of DNA onto the surface of transducers plays an important role in the overall performance of DNA sensors. Electrochemical transducers based on carbon or gold electrodes have been extensively reported for DNA sensors. Gold electrodes can easily accomplish self-assembly *via* gold–thiol interactions, but their high electrochemical active surface is easily inactivated by modification, and their potential window is limited to a relatively positive range due to low overpotential of gold for hydrogen evolution,[3] In contrast, carbon

[a]*Department of Bioelectronics and Biosensors, Alagappa University, Karaikudi-630003, India. E-mail: dharumanudhay@yahooco.in*
[b]*Centro de Nanotecnología Aplicada, Facultad de Ciencias, Universidad Mayor, Santiago-5750, Chile*
[c]*Key Laboratory of Analytical Chemistry for Life Science, School of Chemistry and Chemical Engineering, Nanjing University, Nanjing 210023, P. R. China*
[d]*Institute of Nano Science and Technology (INST), Sector 64, Mohali-160064, Punjab, India. E-mail: rsdey@inst.ac.in*
[e]*Institute of Functional Materials and Agricultural Applied Chemistry, Jiangxi Agricultural University, Nanchang 330045, PR China. E-mail: wenyangping1980@gmail.com*

†Electronic supplementary information (ESI) available (including Synthesis of GO, eqn (1)–(5), Fig. S1–S8, and Table S1–S6). See DOI: 10.1039/c7nr06952a

electrodes have been widely used in the field of electrochemical sensors and have demonstrated a number of advantages such as low cost, abundant structural variety, tailorable surface chemistry, wide potential window, relatively inert electrochemistry, extraordinary electrocatalytic activity, and good conductivity and strength.[5,6] The glassy carbon electrode (GCE) is recognized as the most common carbon electrode. It has a well-defined surface, and various groups have been applied as surface modifiers for different applications. Moreover, GCE assembled/modified by numerous nanocarbon and/or nanometal materials are increasingly used for the highly efficient fabrication of sensors, capacitors and batteries/cells,[7–9] especially electrochemical biosensors for the detection of biomacromolecules.[8,9]

Graphene usually has many defects, which are the most significant obstacles for realizing the superior properties of pristine graphene. A large number of research efforts have focused on reducing these defects to recover the ideal properties of graphene during synthesis. Kim's team[10] demonstrated healing graphene defects using selective electrodeposition. Yoon and coworkers[11] developed self-healing reduced graphene oxide (rGO) films by supersonic kinetic spraying. Park *et al.*[12] reported the defect healing of rGO *via* intramolecular cross-dehydrogenative coupling. D'Elia *et al.*[13] prepared self-healing composites based on the supramolecular polymer in a graphene network for sensing applications. Wang's group[14] investigated an interfacial strengthening and self-healing effect in graphene–copper composites under shear deformation. Clearly, the defects of graphene could be self-healed using different methods.

It is expected that a new strategy with gold nanoparticles (AuNPs) on a transducer surface could improve the sensitivity of DNA hybridization. Cai *et al.*[15] used AuNPs to enhance the immobilization amount of DNA on a gold electrode, which ultimately lowered the detection limit (LOD) of the electrochemical DNA sensor. Ma *et al.*[16] reported a highly sensitive electrochemical DNA sensor based on multifunctional encoded AuNPs on the surface of a nanoporous gold electrode due to the increased amount of immobilized DNA and highly selective hybridization. Recently, the one-step coelectrodeposition of graphene–metal nanocomposites comprising metal nanoparticles (NPs) and rGO has been widely reported for chemo/biosensing applications,[17–19] especially the highly sensitive detection of DNA hybridization using graphene/AuNPs.[7,19–21]

Three-dimensional (3D) nanoarchitectures have attracted tremendous attention for their widespread applications in batteries, supercapacitors, chemo/biosensors, oil sorbents and other electronic and catalysis devices. Layer-by-layer (LBL) assembly has been proven to be an a simple, versatile and significantly inexpensive method for many potential applications in controlled releases, lithium-ion batteries, chemo/biosensing, electro/photocatalysis, field emission, electrochromic devices and energy conversion in storage devices. Xue *et al.*[22,23] built a 3D LBL graphene–nanogold hybrid architecture for electrochemical biosensors. They pointed out that the 3D LBL-modified electrode exhibited higher selectivity and sensitivity compared to graphene, nanogold and their mixture. Moreover, the LBL-assembled technique with a 3D healable structure of nanomaterials increased the electrical and mechanical properties of the flexible electronic device. The organic linker is more stable due to the gold–thiol bond in 3D LBL structures. Hence, a new strategy for the facile preparation of a multilayer nanohybrid thin film based on functionalized nanocarbon and/or nanometal materials with a 3D LBL nanoarchitecture with application in electrochemical biosensors is very necessary.

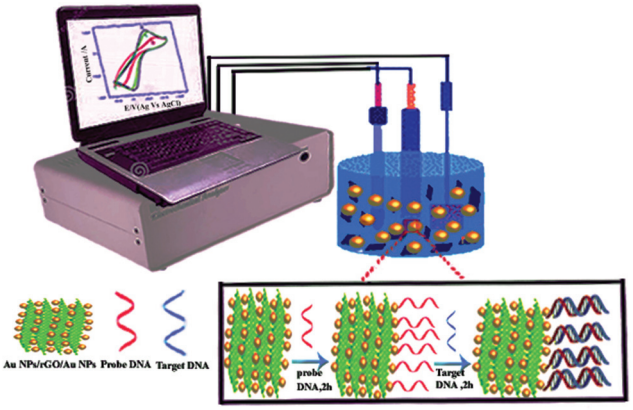

Scheme 1 The one-step coelectrodeposition-assisted LBL assembly of self-healing 3D AuNPs/rGO/AuNPs/GCE for ultrasensitive sensing of DNA hybridization.

Inspired by previous studies, we focused on proposing a new and highly efficient strategy for the facile fabrication of an innovative ultrasensitive electrochemical DNA sensing platform with a 3D LBL nanoarchitecture based on an alternate multilayer nanohybrid thin film of both AuNPs and rGO using one-step electrodeposition-assisted LBL assembly (Scheme 1). It is worth mentioning that the one-step electrochemical simultaneous reduction of both graphene oxide (GO) and the Au precursor was achieved, and an alternate multilayer nanohybrid thin film of AuNPs/rGO/AuNPs with self-healing properties and a 3D LBL nanoarchitecture was obtained. This film was characterized by scanning electron microscopy (SEM), atomic force microscopy (AFM), different Fourier transform infrared spectra (FTIR), X-ray powder diffraction (XRD), X-ray photoelectron spectroscopy (XPS), electrochemical impedance spectroscopy (EIS), cyclic voltammetry (CV) and computational calculations. $Fe[(CN)_6]^{3-/4-}$ was employed as a redox probe to fabricate an impedance sensing platform for the label-free ultrasensitive electrochemical detection of DNA hybridization.

2. Results and discussion

2.1. Characterization of the 3D AuNPs/rGO/AuNPs

All the films were electrodeposited onto the GCE surface by CV (Fig. 1a), and their morphologies were recorded by SEM (Fig. 1b–f). Clearly, many AuNPs were electrodeposited on the

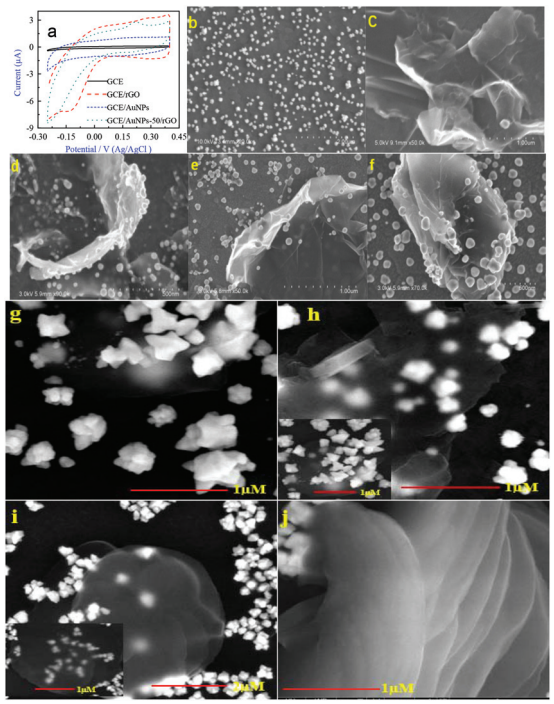

Fig. 1 (a) CVs (a) of electro-reduction of GO and/or $AuCl_3^-$ on the surface of the GCE in 0.5 M H_2SO_4 at a scan rate of 50 mV s^{-1}. SEM images of: AuNPs (b), rGO (c), AuNPs/rGO/AuNPs-10 (d), 30 (e) and 50 cycles (f). Field emission SEM images of AuNPs/rGO/Au with 10 (g), 30 (h), and 50 cycles (i and j).

surface of the substrate electrode by the electroreduction of Au^{3+}, and only a few nanoparticles formed larger clusters (Fig. 1b). Similarly, some rGO nanosheets displayed an intensely crumbled and folding wrinkle structure, revealing that rGO with an ultrathin layer was electrodeposited on the surface of the substrate electrode by the effective electroreduction of GO (Fig. 1c). The layered-structured films with the potential for 10, 30 and 50 cycles were named as AuNPs/rGO/AuNPs-10, AuNPs/rGO/AuNPs-30 and AuNPs/rGO/AuNPs-50, respectively (the mixed film with the potential for 10, 30 and 50 cycles were named as rGO–AuNPs-10, rGO–AuNPs-30 and rGO–AuNPs-50, respectively). It is imperative to note that the number of cycles during the continuous electroreduction had a significant impact on the morphology of the co-deposited materials on the GCE surface (Fig. 1d–f). Field emission SEM further revealed that the AuNPs seemed to be intercalated into the layered-structured rGO, and a GO/AuNPs hybrid film with a 3D LBL structure was formed (Fig. 1g–j). In addition, the layered-structured GO/AuNPs hybrid thin film seemed to be formed after the successive electroreduction after 10 cycles, (Fig. 1g). A large number of AuNPs appeared on the surface of rGO (Fig. 1h) after the successive electroreduction after 30 cycles, but a small amount of AuNPs were still clearly seen under the thin layer of rGO in the top view of the field emission SEM images in Fig. 1g and h. The GO/AuNPs hybrid with a 3D LBL structure can be clearly observed from the top and side views of the field emission SEM images after 50 successive electroreduction cycles in Fig. 1i and j. Surprisingly, the layered-structured film synthetized by the new method (AuNPs/rGO/AuNPs-50) was remarkably different from the mixed film formed *via* the traditional method (rGO–AuNPs-50, Fig. S1†), as it could be observed that many larger spherical particles were distributed on the surface of the substrate electrode using the novel method (Fig. S1a†). It was also observed that the reduction peak of rGO was shifted to negative potentials towards high pH, indicating that H^+ was involved in the reduction process of rGO.[24] The reduction peak of rGO disappeared after 50 cycles (Fig. 1a), thus showing the completion of rGO reduction on the GCE surface.

The reduction of Au(III) to Au (0) appeared at approximately 0.1 V (Fig. 1a), which had been positively shifted to increase the potential cycling.[25] Fig. S2† represents the CV behaviours of different thin-film-modified ITO electrodes in 0.5 M H_2SO_4. The ITO/rGO electrode shows an obvious increase in current compared to the ITO electrode, which is related to the relatively better conductivity of rGO. The ITO/AuNPs electrode presented two pairs of redox peaks, ascribed to the oxidation–reduction behaviours of AuNPs. The ITO/AuNPs/rGO/AuNPs-50 electrode had a lower current intensity associated to the two pair of redox peaks of AuNPs, which could be attributed to the relatively weak conductivity of rGO after the electroreduction. The obvious increase in the reduction peak current in the different modified electrodes (Fig. 1a) was associated with the electroreduction of both GO and/or Au^{3+} in H_2SO_4. Interestingly, the presence of negatively charged $AuCl_3^-$ stabilized the reduction of GO and allowed the co-electrodeposition onto the GCE surface.

The AFM image of rGO with 50 cycles in the absence of $HAuCl_4$ showed a wrinkled morphology of multilayer graphene (Fig. 2a), while the AFM image of AuNPs with 50 cycles in the absence of rGO presented a homogeneous distribution of spherically shaped AuNPs (Fig. 2b). The morphology of AuNPs/rGO/AuNPs-50 (Fig. 2c) was different from rGO–AuNPs-50 (Fig. 2d), and its AFM image showed a 3D architecture (Fig. 2e) in combination with the 3D architecture of AuNPs (Fig. 2f). In addition, topological images of AuNPs/rGO/AuNPs with 10, 30 and 50 cycles are presented in Fig. S3.† The AFM images of LBL AuNPs/rGO/AuNPs revealed that the height of the profile and the thickness were increased (5.2 to 36.1 nm). Fig. 3a depicts the deconvoluted C 1s spectra of GO containing five C 1s peaks (C=C at 284.3 eV, C–OH at 285.7 eV, C–O–C at 286.6 eV and O–C=O at 288.7 eV). The increasing intensity of the peak at 284.5 eV formed in the C 1s spectra of rGO revealed the higher number of C=C bonds after the electroreduction (Fig. 3b). The deconvoluted C 1s spectra of AuNPs/rGO/AuNPs-50 showed that the high intensity peak (Fig. 3c) is located at a lower binding energy (282.5 eV) due to the C–H coupling and less conjugated π system, influenced by the H^+ reduction.[26–30] The wide scan XPS spectrum further confirmed the presence of C, O and Au in AuNPs/rGO/AuNPs-50 (Fig. 3c), and the relative atomic percentage of GO, rGO and AuNPs/rGO/AuNPs-50 in Table S1† also confirmed the reduction of GO and the pres-

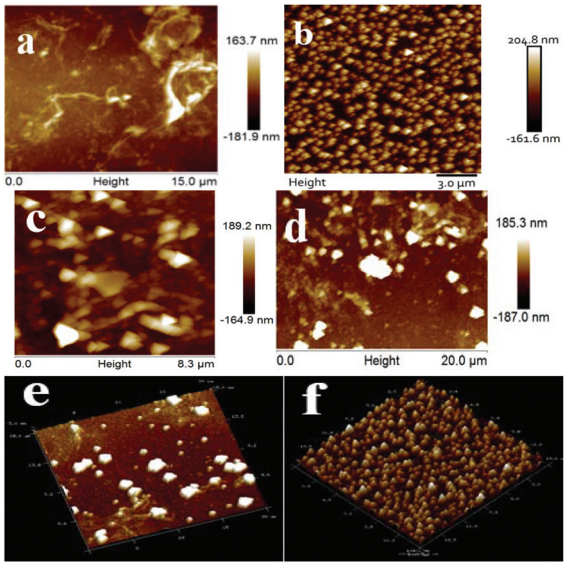

Fig. 2 AFM images of: rGO-50 (a), AuNPs-50 (b), AuNPs/rGO/AuNPs-50 (c), rGO–AuNPs-50 (d), 3D AuNPs/rGO/AuNPs-50 (e), and 3D AuNPs-50 (f).

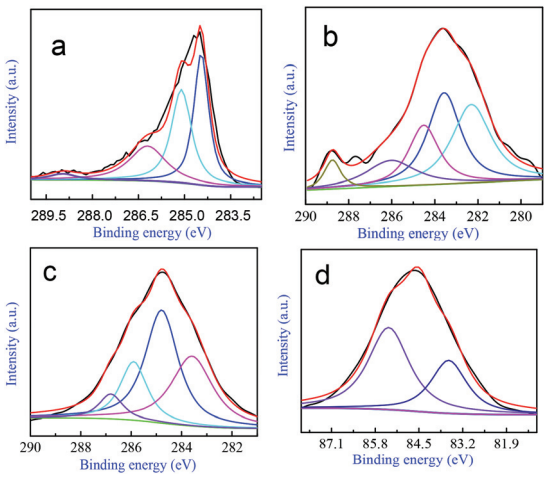

Fig. 3 Deconvoluted XPS spectra of carbon 1s for: (a) GO, (b) rGO, (c) 3D AuNPs/rGO/AuNPs-50 and of Au 4f (d).

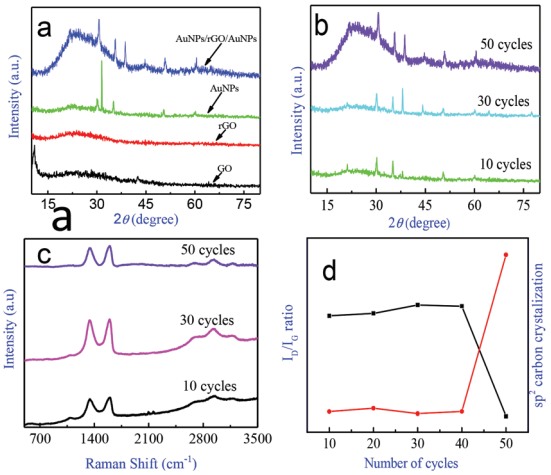

Fig. 4 XRD patterns of different films with GO, rGO, AuNPs, 3D AuNPs/rGO/AuNPs-50 (a), and AuNPs/rGO/AuNPs with 10, 30 and 50 cycles (b). Raman spectra of AuNPs/rGO/AuNPs (c) and variation of the I_D/I_G ratios and sp^2 carbon crystalline size with 10, 30 and 50 cycles (d).

ence of C, O and Au in AuNPs/rGO/AuNPs. The high-resolution XPS spectrum of Au (Fig. 3d) showed two peaks for Au 4f 7/2 and Au 4f 5/2, centred at 83.7 eV and 87.0 eV, respectively, which were in accordance with the previous reports for Au.[1,9] It could be concluded that Au^{3+} was effectively reduced on the surface of GO nanosheets, as evidenced by the blue shift of Au 4f induced by the electron transfer from rGO to AuNPs.[9,14] Also, the XRD results were in agreement with the high-quality crystalline structure of different films (Fig. 4a). The evolution of the talline structure was revealed in Fig. 4a. The XRD patterns of AuNPs displayed standard crystalline values of the gold atom (JCPDS 04-0784). A sharp peak appeared at 10.8° for GO, but this peak completely disappeared, and a broad peak centred at around 21.2° was observed for rGO onto ITO. The small peaks at 30.57°, 35.32°, 49.58° and 50.85° were assigned as the characteristic peaks of ITO (JCPDS File no. 89-4599).[31] The volume-averaged particle size was calculated using the Scherrer equation, and the FWHM of the G band of the (111) peak was 1.41 nm for GO, 16.91 nm for rGO and 4.3 nm for AuNPs/rGO/AuNPs, respectively. Fig. 4b shows the XRD pattern for AuNPs/rGO/AuNPs with 10 and 30 cycles. The (002) peak at 10.8° has disappeared, indicating that AuNPs grew on the surface of graphene nanosheets with increasing time, which prevented the restacking of graphene nanosheets.[14,15] The *d*-spacing for these films decreased from 0.2 to 0.3, confirming the formation of high-quality graphene nanosheets.[34] The appearance of the peak at 21.23° corresponded to the face-centred cubic structure for AuNPs/rGO/AuNPs-50, suggesting the successful attachment of AuNPs to the surface of the pristine-graphene sheets (Fig. 4b). It was previously observed that the electrochemical durability of carbon depended on its graphitic properties.[21] There were two main reasons for this, as follows. First, the corrosion of carbon usually starts from structural defects, but carbon with a greater graphitic phase has lesser defects.[25,26,34] Second, highly graphitic carbons supplied the catalyst with more electron channels during the electrocatalytic reaction. Thus, the electrodeposition with 50 cycles was the optimal condition for the preparation of AuNPs/rGO/AuNPs/GCE with the 3D alternate-layered nanoarchitecture. The Raman Fourier transform infrared spectra (RFTIR) of GO, rGO and rGO/AuNPs-50 are shown in Fig. 5a. GO characteristic vibration peaks were observed at 1303 cm^{-1} and 1603 cm^{-1}, corresponding to sp^2 and sp^3 carbons, whereas the hydrocarbon peak appeared at 2219 cm^{-1}, which was observed from two major peaks corresponding to the C–H bending frequency (551 cm^{-1}) and from hydrogen on the benzene (1083 cm^{-1}) from the electrochemically reduced GO (Fig. 5a). The AuNPs/

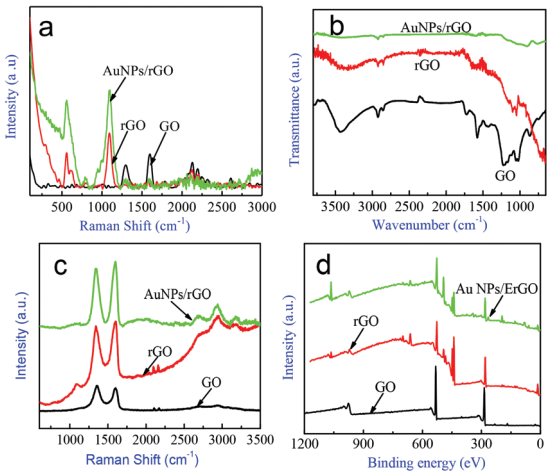

Fig. 5 Raman-FTIR spectra (a), ATR-FTIR spectra (b), Raman spectra (c), and wide scan XPS spectra (d) of GO, rGO and 3D rGO/AuNPs-50.

rGO-50 had three bands for the CH out of plane bending, the substituted hydrogen on the benzene rings and from the physical adsorption at C–OH 793, 1065 and 3142 cm^{-1}, indicating that the epoxide group and carbonyl group were removed after the reduction process.[33] To get further information about the conformation, attenuated total reflectance Fourier measurements were taken (Fig. 5b). GO bands were observed at 1070 cm^{-1} (hydroxide), 1240 cm^{-1} (epoxide), 1572 cm^{-1} (C=C), 1431 cm^{-1} (carbonyl), 1725 cm^{-1} (carboxylic acid and carbonyl moieties), 2848 cm^{-1} (bending mode of C–H in the benzene ring methylene group asymmetric), 725 and 920 cm^{-1} (C–H out of plane bending in the benzene ring of graphene) and 3425 cm^{-1} (free hydroxide),[34] respectively. These results were supported by the appearance of characteristic vibrations for epoxy and hydroxyl groups and saturated C–H vibrations for sp^3 hybridized carbons. The interaction between AuNPs and rGO decreased the band intensities of C=O (1715 cm^{-1}), the OH mode (1045, 1425 and 3425 cm^{-1}) and the C–C stretching mode (1240 cm^{-1}). AuNPs/rGO-50 showed bending modes only at 746 and 890 cm^{-1}. This evidence was further supported by the large decrease in peak intensities of the composite with 50 cycles (Fig. 5b). The peak intensities of the bending mode of C–H in the benzene ring and methylene group (symmetric and asymmetric) at 2848 and 2935 cm^{-1} were reduced for AuNPs/rGO/AuNPs-10 and AuNPs/rGO/AuNPs-30, respectively. However, an additional peak at 790 cm^{-1} appeared only for AuNPs/rGO/AuNPs-50. This confirmed the fact that hydrogen atoms in graphene preferred to be chemisorbed on neighbouring carbon atoms on the other side of the graphene nanosheets, which changed the hybridization of carbon atoms from sp^2 to sp^3, resulting in the elongation of C–C bonds in rGO.[26] Hydrogen atoms tended to react on both surfaces of the pristine graphene and AuNPs–rGO. As indicated by the Raman spectra (Fig. 5c), the band at 790 cm^{-1} was related to the out of plane bending of the aromatic C–H with different degrees of substitution on graphene edges due to the increasing sp^3 carbons.[16] The disappearance of the stretching frequency at 1642 cm^{-1} was attributed to rGO, implying that a large fraction of the O–H group was removed.[27] Hence, the complete reduction of GO was impossible at pH ≤2. GO showed two characteristic peaks at 1338 cm^{-1} and 1598 cm^{-1}, respectively, corresponding to the D and G bands, whereas the rGO showed four major peaks around 1338, 1596, 2693 and 2932 cm^{-1}, respectively, which were attributed to the D, G, 2D and (D + G) bands, respectively (Fig. 4c). The G band was analogous to an E2g mode of graphite, which appeared for the in-plane bond stretching vibration of sp^2 bonded carbon atoms.[4,9,10] Kudin *et al.*[27] reported that graphite carbons with the G peaks position had not changed for the rGO. This evidence was related with graphite self-healing, which was reflected in the restoration of the in-plane sp^2 hybridization. The D band at 1338 cm^{-1} corresponded to the breathing mode of k-point phonons of A1g symmetry with vibrations of carbon atoms and dangling bonds in plane terminations of the disordered sp^3 carbon in sp^2 lattice defect crystalline graphitic materials.[4] The 2D band at 2691 cm^{-1} was observed for the second-order band of zone-boundary phonons. The D + G band at 2923 cm^{-1} in rGO confirmed the hydrogenation during the reduction process and the formation of sp^3 C–H bonds or the saturation of the –C=C– bonds by H atoms (Fig. 4b).[26] The decreasing I_D/I_G suggested that the decreasing amount of defects led to the enhanced electronic conduction. The decreasing crystal sizes of GO, rGO and rGO/AuNPs-50 were 16.94, 16.78 and 15.3 nm, respectively (Fig. 5c). The I_D/I_G ratios for rGO/AuNPs with different cycles (10, 30 and 50) are listed in Table S2.† The in-plane crystalline size (La) of the sp^2 graphene was calculated using eqn (1).† The lower crystal size (15.3 nm) suggested that a lower amount of defects was introduced in the AuNPs/rGO/AuNPs-50 in comparison to AuNPs/rGO/AuNPs-10 and AuNPs/rGO/AuNPs-30. The I_D/I_G ratios increased with the increasing number of cycles of electrodeposition, which were further supported by the increasing FWHM of the G band, suggesting the increased size of the sp^2-ring domains and reduced sp^3 fraction. The variation of I_D/I_G ratios from 0.1 to 1 indicated the nature of the layer stacking of graphene sheets. The lower I_D/I_G ratio of 0.13 for AuNPs/rGO/AuNPs-50 demonstrated the electrodeposition of a single graphene layer (Fig. 4c and d). The decrease in I_D/I_G ratios and the increase in the crystalline size of AuNPs/rGO/AuNPs (its suspension was I_D/I_G = 0.62) indicated that the deposited AuNPs/rGO/AuNPs film was smaller (Table S2†). The dissociation of C–C bonds led to the point-defect formation of electrodeposited films. AuNPs grew on the rGO surface, first randomly distributed with hydrogen ions and C–C bond dissociation, allowing the healing of defects. Meanwhile, the reduction removed the oxygen functional groups of GO, and the healing of their structural defects occurred simultaneously.[26–30] Zhao *et al.*[31] proposed the introduction of hydrogen atoms, where oxygen was bonded with carbon atoms forming larger holes. The oxygen and hydrogen paired to create a hydroxyl group, leaving behind the lattice to heal the hole. Bandodkar *et al.*[32] reported that the $Nd_2Fe_{14}B$ micro/

nanoparticle composite graphite layers attained self-healing capabilities when applied in printed electromagnetic devices. The CV redox behaviour was slightly shifted at higher scan rates and increased the efficient electron-transfer properties, which could be related to the self-healing effect. As shown by the CV in Fig. S4,† the consequence of this self-healing effect in the AuNPs/rGO/AuNPs composite was associated with the improvement in its electro-activity. The crystalline nature of graphene was also revealed from the FWHM of the Raman bands. Its smaller FWHM value is better than for the crystalline structure, because the graphitic disorder effect is decreased owing to the increase in the number of new sp^2 carbon atoms.[35,36] The behaviour of the trends of the I_D/I_G ratios and FWHM values confirmed the aromaticity of the sp^2 hybridized carbon. The crystalline nature of graphene was improved below 50 cycles. This was further reflected by the large La value of 146 nm for AuNPs/rGO/AuNPs-50 compared with the lower value of La of 16.9 nm for AuNPs/rGO/AuNPs with 10 or 30 cycles.[37] Although the hydrogen functionalization occurred at the –C═C– bond, which was a more active plane for GO networks, the hydrogenation changed the hybridization of carbon atoms from sp^2 to sp^3, resulting in larger C–C bonds in the H-modified graphene. Hydrogen atoms tended to react with surfaces of the plane in pristine graphene. The transition from bulk graphite to nano-graphite, and *vice versa*, produced a pronounced effect in the Raman spectra, especially with the intensity ratio of the D and G band, I_D/I_G. The smaller the crystalline grains were, the higher the I_D/I_G ratio was, and the FWHM of the G band decreased for GO and rGO. A decrease in the average size of the sp^2 domains upon reduction of the GO occurred, in which new graphitic domains were created with smaller sizes than the ones present in GO before reduction, although in larger quantities. Therefore, although there were more defect-free sp^2 carbons after reduction, these carbons formed smaller domains than those in the GO, which led to large quantities of structural defects.[25] Another possible reason was the increasing fraction of graphene edges, which could also contribute to the increase in I_D/I_G ratios.[32] The decreased I_D/I_G ratios for GO, rGO and AuNPs/rGO/AuNPs-50 (Table S2†) indicated the self-healing defects due to the increasing crumbled structure and an improving electrocatalytic activity. GO/AuNPs-50 with high conductivity revealed that the interaction between AuNPs and rGO is too weak to absorb Au atoms on the rGO surface, which depended on their electrodeposition time.

2.2. Computational calculations of the 3D AuNPs/rGO/AuNPs film

The isolated rGO structure was fully optimized at the B3LYP/6-31G level and used as a reference for the calculation of the BSSE-corrected interaction energy (E_{int}). Fig. 6a shows the optimized rGO geometry. rGO has some potential coordination sites with high electron density, where Au_2 could be attached and generate complexes. Starting geometries of the Au_2/rGO complexes for the optimization were generated by placing the Au_2 near the electron-rich sites of the structure. Three

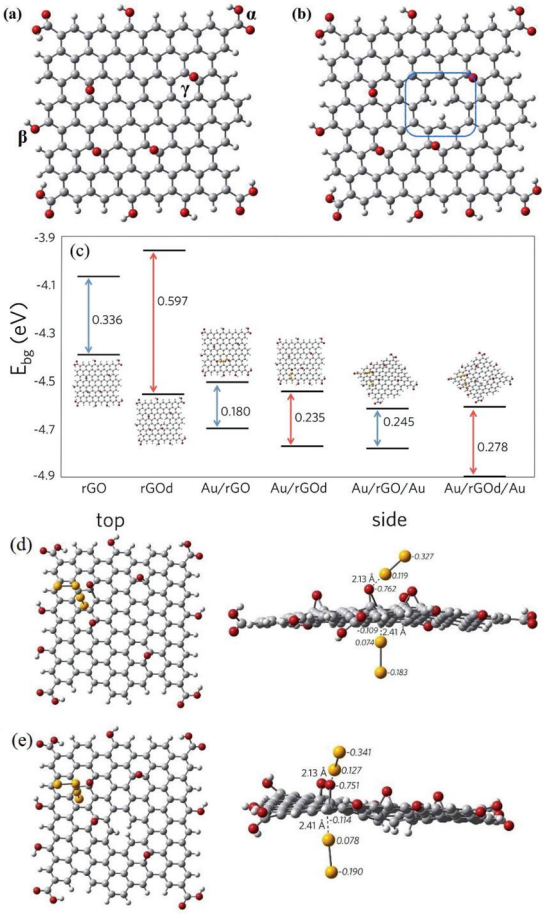

Fig. 6 Optimized structure at the B3LYP/6-31G level of rGO (a) and defective rGO (rGOd) with three possible coordination sites (α, β and γ) (b). (c) Theoretical energy band gap calculated for different optimized complexes of rGO (—) and rGOd (—) with Au_2. Ground-state structures of the (d) Au_2/rGO/Au_2, and (e) Au_2/rGOd/Au_2 complexes optimized at the B3LYP/6-31G//LANL2DZ level. NPA charges (a.u.) for selected atoms are displayed in italics, and bond lengths in Å.

different coordination sites were considered (Fig. 6a): Au_2 interacting with (α), the carboxylic acid group (–COOH), and (β), the hydroxyl group (–OH) at the edges of the rGO layer, as well as (γ), the epoxy groups (–O–) on the rGO layer. Three initial conformations were tested at each coordination site to search for alternative local minima. Table S5† lists the most stable E_{int} at each coordination site, the distances between the Au_2 and the anchor atom, and the charge for the three optimized complexes. The E_{int} indicated that the most stable Au_2/rGO complex corresponded to site (γ), then (α) and finally (β). Complex (γ) was the only structure with a coordination related to the surface of the rGO layer mediated by the –O– moieties. Complexes (α) and (β) had coordination to functional groups at the edges of the rGO layer. Fig. S5† shows the optimized geometry of the complexes, in which the bond lengths and NBO charges at selected atomic sites are depicted. System (γ) was approximately 8.6 kcal mol^{-1}, which was more stable than (α), indicating that the presence of the Au nanocluster

improved the delocalization of electronic charge around rGO rings. The Au–O anchor bond distances (dx–Au) followed the opposite tendency of E_{int}. Complex (γ) had the smallest bond length of the set, associated with a stronger interaction and stability. When the total NPA charge of the Au_2 cluster ($\Delta q_{cluster}$) was analysed, it could be noticed that there was a charge transfer from the ligand rGO to the Au_2 cluster in all cases. The largest amount of electron density was transferred in complex (γ), which was approximately 11% more charge than the amount transferred to complex (α). As can be seen from the electrostatic potential surface (EPS) and the frontier molecular orbitals of the optimized structure of rGO (Fig. S6†), most of the electronic density is located at the oxygen atoms belonging to epoxy functional groups. This evidence indicates that the lone pairs of oxygen atoms in the epoxy moieties are highly available for the interaction with metal atoms. According to these results, AuNPs will tend to grow close to –O– on the surface of the rGO layer rather than at the functional groups located at the edge sites of rGO. Once the most stable coordination site was established, the defective rGO (rGOd) structure (Fig. 6b) was optimized at the B3LYP/6-31G level of theory to study the effect of this modification on the conductivity of the system. As Fig. 6c shows, a defect on the surface of rGO produces immediately a considerable decrease in the conductivity in comparison with the original rGO surface, with an E_{bg} of almost twice the value of the original system.

With the aim of exploring the effect of Au in the conductivity of both systems, the Au_2/rGOd complex was optimized, considering the epoxy group as the anchoring site. The E_{int} value of the ground-state geometry of the Au_2/rGOd complex was quite close to the Au_2/rGO structure (Table S3†), revealing similar bond distances and charge values. When E_{bg} was analysed, the value for the Au_2/rGOd system was only 0.055 eV, which was larger than that for the Au_2/rGO complex. In both systems, the energy band gap decreased with the coordination of the Au cluster, but in the case of rGOd, the presence of Au considerably stabilized the system, with an energy band gap approximately 60% lower than the sole rGOd structure, being almost at the same level of the conductivity of the Au_2/rGO layer without defects. Therefore, it is possible to state that the presence of Au_2 allows a healing of the structural defects of rGO, thus improving dramatically the conductivity of the system. This theoretical evidence is in accordance with the experimental result mentioned above.

Finally, a second Au_2 nanocluster was introduced to the system to simulate the 3D LBL AuNPs/rGO/AuNPs surface. Fig. 6d and e show the optimized geometries of both rGO and rGOd complexes with two Au_2 clusters. In both cases, E_{int} was higher than the value registered in systems with one Au_2 cluster (Table S3†), and had a difference of only approximately 2 kcal mol^{-1} between the normal and defective rGO structure. Moreover, the bond distances and the charge distribution were also very similar. On the other hand, $\Delta q_{cluster}$ increased about 35% in comparison to systems with only one Au_2 cluster, indicating that a higher amount of electronic density was transferred to the Au cluster. This evidence confirmed that the presence of a second coordinated Au_2 cluster reinforces the interaction and has a stabilizer effect in defective surfaces of rGO.

2.3. 3D AuNPs/rGO/AuNPs/GCE for an ultrasensitive DNA sensor

CV and EIS were selected to study biorecognition events at the bioelectrode interface. An extremely sensitive, non-destructive, label-free electrochemical biosensing method was used for the assay of DNA hybridization. $[Fe(CN)_6]^{3-/4}$ was selected as the redox probe because of its high sensitivity to the surface behaviours of different materials-modified GCEs. The peak currents (Fig. 7a–c), ΔE_p (Fig. 7a–c) and R_{ct} (Fig. 7e–g) of the GCE/AuNPs/rGO/AuNPs with the potential for 10, 30 and 50 cycles were very close to that of GCE, suggesting that the good electrochemical activity and electroconductivity of 3D LBL AuNPs/rGO/AuNPs hybrid composite film were because of the formation of both AuNPs and a 3D LBL-assembled nanoarchitecture and the electroreduction of the functional groups of

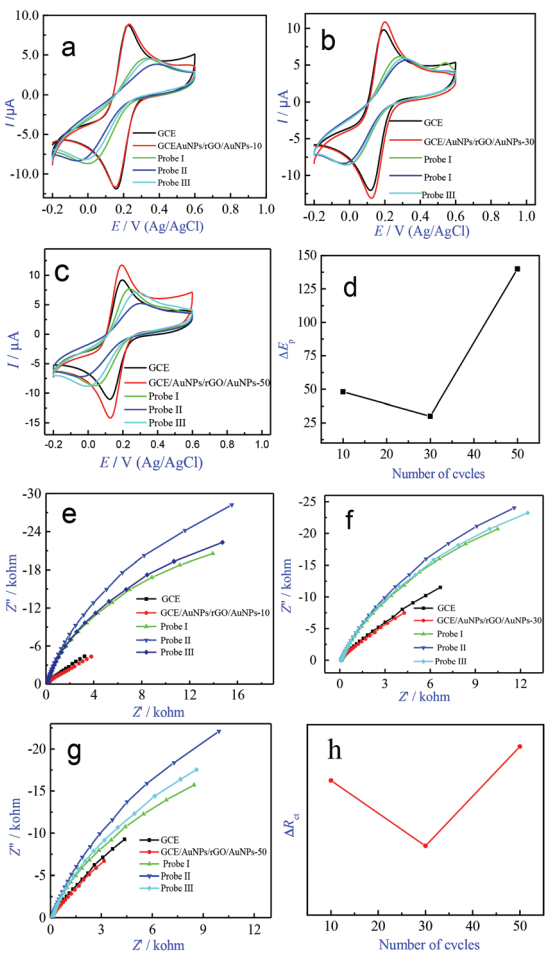

Fig. 7 CVs (a–c) and EIS behaviours (e–g) of the bare GCE, AuNPs/rGO/AuNPs/GCE with different cycles and their probes: probe I, probe II and probe III recorded in PBS containing 1 mM $[Fe(CN)_6]^{3-/4-}$ at a scan rate 50 mV s^{-1}. The relationship between ΔE_p (d) and ΔR_{ct} (h) of probe II with different cycles.

GO. Probe I was formed by immobilizing the capture DNA onto the surface of GCE/AuNPs/rGO/AuNPs after different cycles, which resulted in an increase in both ΔE_p (Fig. 7a–c) and ΔR_{ct} (Fig. 7e–g), a decrease in peak currents (Fig. 7a–c) due to the introduction of non-conducting ssDNA, and in electrostatic repulsion between the negative charge of phosphate backbones of the ssDNA-modified electrode and redox probe $[Fe(CN)_6]^{3-/4-}$, suggesting that the capture DNA was successfully linked into the GCE/AuNPs/rGO/AuNPs-50 (*i.e.* the formation of probe I). Probe II was formed when probe I was used to hybridize with cDNA, which further enlarged both ΔE_p (Fig. 7a–c) and R_{ct} (Fig. 7e–g) and decreased the peak currents (Fig. 7a–c), indicating a further increase in the non-electroconductivity of dsDNA on the electrode surface and a further enhancement in the electrostatic repulsion between the negative charge of the phosphate backbone of the dsDNA-modified electrode and $[Fe(CN)_6]^{3-/4-}$. However, probe III was formed when probe I was used to hybridize with ncDNA, with negligible changes in the peak currents (Fig. 7a–c), ΔE_p (Fig. 7a–c) and R_{ct} (Fig. 7e–g), suggesting the excellent selectivity of the fabricated DNA sensor.

The apparent diffusion coefficient (D') could be correlated with the real electroactive surface area being different from the geometric one in modified electrode systems. The D' values for different modified electrodes can be calculated by the Randles–Sevcik equation (eqn (2)).† The D' values were 2.83×10^{-4} cm^2 s^{-1} at the GCE, 3.21×10^{-4} cm^2 s^{-1} at the GCE/rGO, 4.47×10^{-4} cm^2 s^{-1} at the GCE/AuNPs and 3.56×10^{-4} cm^2 s^{-1} at the GCE/AuNPs/rGO/AuNPs-50, respectively. This revealed that different materials-modified GCEs increased the electroactive surface area owing to the introduction of nanomaterials with a large specific surface area and high current response of the modified electrode with high electroconductivity (Fig. 8a and b). The D' values at the GCE/AuNPs/rGO/AuNPs with 10, 30 and 50 cycles were 3.2×10^{-4}, 3.56×10^{-4} and 6.04×10^{-4} cm^2 s^{-1}, respectively. The D' values increase with increasing cycles revealed the increase of both the electroactive surface area and electroconductivity of the GCE/AuNPs/rGO/AuNPs because of the formation of a 3D LBL-assembled nanoarchitecture. The apparent heterogeneous electron-transfer rate constants (K'_{et}) at different modified electrodes were calculated using eqn (3).† The K'_{et} values were 1.99×10^{-3} at the GCE, 5.61×10^{-3} at the GCE/rGO, 4.01×10^{-3} cm^2 s^{-1} at the GCE/AuNPs and 2.24×10^{-3} cm^2 s^{-1} at the GCE/AuNPs/rGO/AuNPs-50, whereby the increases of K'_{et} at the different-materials-modified GCE revealed the enhancement of the heterogeneous electron-transfer properties, indicating that the decrease in electronic transfer resistance was due to the increase in the electroconductivity of the different modified materials. The K'_{et} values at the GCE/AuNPs/rGO/AuNPs with 10, 30 50 cycles were 4.83×10^{-4} cm^2 s^{-1}, 2.84×10^{-4} cm^2 s^{-1} and 2.24×10^{-3} cm s^{-1}, respectively. GCE/AuNPs/rGO/AuNPs with increasing cycles revealed an increase in both electronic transfer resistance and the electroactive surface area of 3D LBL GCE/AuNPs/rGO/AuNPs. According to the Nicholson equation (eqn (4)),† the formal potential heterogeneous charge transfer rate constant (K'_{app}) was calculated to be 1.09×10^{-3} cm s^{-1} at the GCE, 2.35×10^{-3} cm s^{-1} at the GCE/rGO, 1.14×10^{-3} cm s^{-1} at the GCE/AuNPs and 1.06×10^{-3} cm s^{-1} at the GCE/AuNPs/rGO/AuNPs-50. Nicholson voltammetry theory for electron kinetics revealed the effect of the electroconductivity of the different modified materials on the reversible electron-transfer reaction. The K'_{app} values at the GCE/AuNPs/rGO/AuNPs with 10, 30 and 50 cycles were 1.25×10^{-3}, 1.11×10^{-3} and 1.06×10^{-3} cm^2 s^{-1} (Table S3†), respectively. The K'_{app} values decreased with the increasing number of cycles, which led to a fast reversible electron-transfer reaction between $[Fe(CN)_6]^{3-/4-}$ and the modified electrode interface due to the relatively small ΔE_p.

To optimize the cycling numbers of the AuNPs/rGO/AuNPs/GCE, parameters such as the peak currents, ΔE_p, D', K_{et} and K_{app} of the GCE/AuNPs/rGO/AuNPs with different cycles, need to be considered, and are given in Tables S3 and S4.† The peak currents and D' values of the 3D LBL GCE/AuNPs/rGO/AuNPs gradually increased with the increase in the number of cycles due to the increase in the thin film size of the modified layers on the GCE surface. The ΔE_p, K_{et} and K_{app} values of the 3D LBL GCE/AuNPs/rGO/AuNPs gradually decreased with increasing the number of cycles (Tables S3 and S4†), suggesting a fast reversible electron-transfer reaction between $[Fe(CN)_6]^{3-/4-}$ and the modified electrode interface. The increasing surface volume ratio and decreasing D value with the gradual attainment of a dense structure could explain the increasing K_{app} values from the impedance spectrum.[38] However, the introduction of AuNPs effectively increased the conductivity of rGO by leading to an effective chemical healing of the defects, which was supported by the Raman spectra of these films[32] and by computational calculations. In addition, the reproducibility of the electrodes was evaluated in $[Fe(CN)_6]^{3-/4-}$ containing KCl. The nine AuNPs/rGO/AuNPs/GCE were tested independently, and their RSD values for the anodic peak currents and catho-

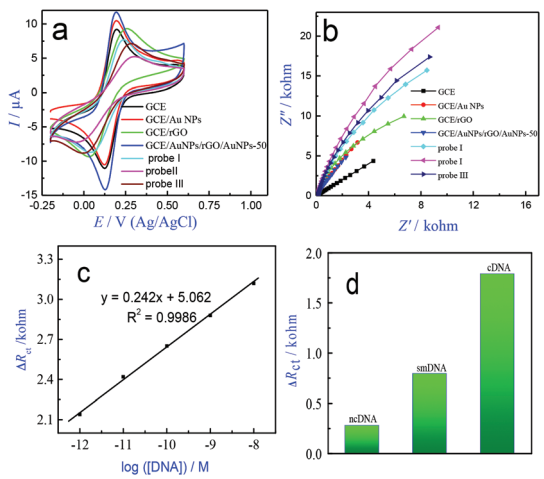

Fig. 8 CVs (a) and EIS (b) of the bare GCE, GCE/AuNPs, GCE/rGO, GCE/AuNPs/rGO/AuNPs-50, probe I, probe II and probe III in the presence of $[Fe(CN)_6]^{3-/4-}$. Linear relationship between ΔR_{ct} and the logarithm of DNA concentration (c). ΔR_{ct} plots of probe I hybridized with different ssDNA (d) with the target concentration of 1×10^{-10} M (n = 3).

dic peak currents were 1.8% and 1.7%, respectively, indicating good reproducibility of the prepared electrode (Fig. S7†). CV and EIS of the GCE/AuNPs/rGO/AuNPs-50 with ssDNA (probe I) before and after hybridization with the cDNA (probe II) and ncDNA (probe III) were measured in the presence of 1 mM $[Fe(CN)_6]^{3-/4-}$ (Fig. 8a and b). Ambrosi *et al.*[39] reported that graphene-based materials could be improved by the charge resistance on more oxygenated species (carboxyl, epoxy and hydroxyl), which has been utilized for easily functionalized biomolecules with high precision and a reproducible order to achieve DNA hybridization for EIS techniques. Due to these advantages, rGO was used in a LBL multilayer to achieve a high sensitive detection of DNA hybridization as a low cost and simple method to prepare an ultrathin film and reusable device. A single layer of graphene has a very low surface charge density compared to a few layers of graphene and also has a uniform coverage, which decreases the charge transfer resistance on the electrode surface. DNA hybridization was examined using GCE/AuNPs/rGO/AuNPs with different numbers of cycles (Tables S3 and S4†). In combination with Raman spectroscopy and XPS, the GCE/AuNPs/rGO/AuNPs-50 showed a larger discrimination effect related to the reduction of the pinhole size between the ssDNAs, which restacked the diffusion through the film.[1,10,40] The as-fabricated DNA sensor with 50 cycles was further examined for the effects of the target concentrations (Fig. S8†).

The impedance behaviours of the capture ssDNA immobilized onto the GCE/AuNPs/rGO/AuNPs-50 (probe I) with the various concentrations of cDNA are presented in Fig. S8.† The logarithm of DNA concentration *vs.* ΔR_{ct} plots exhibit a dynamic linear range from 0.1×10^{-6} to 1×10^{-13} M (Fig. 8c). The limit of detection (LOD) was calculated by LOD = 3 s m^{-1}, where s is the standard deviation (three runs) of the linear range and m is the slope of the linear equation in Fig. 8c. The calculated LOD was 3.64×10^{-14} M. As listed in Table S6,† the as-fabricated DNA sensor displayed the widest linear range and lowest LOD in comparison with previous reported electrochemical DNA sensors based on AuNPs and/or GO.

The selectivity of the electrochemical hybridization assay was investigated using probe I. Different ssDNA sequences, like cDNA, ncDNA or smDNA, were used to hybridize with probe I. Fig. 8d presents a two-fold increase in R_{ct} for cDNA, a 10% increase in R_{ct} for ncDNA and a 40% increase in R_{ct} for smDNA. These results confirmed the development of a highly selective DNA sensor. The analytical signal of cDNA could also be clearly observed in the presence of a 100-fold excess of smDNA (Fig. 8d), indicating that the fabricated biosensor displayed excellent selectivity for cDNA in the presence of excess smDNA. In addition, the feasibility and practicability of the AuNPs/rGO/AuNPs/GCE with the capture ssDNA (probe I) was evaluated in different samples containing ncDNA or/and smDNA using the standard addition method. Their recovery values and relative standard deviation were no more than 5%, which were within the acceptable range, revealing that the proposed method was feasible and applicable for future applications in real samples.

3. Conclusions

A AuNPs/rGO/AuNPs multilayer thin film with a 3D LBL-assembled nanoarchitecture was facilely fabricated by simultaneous electroreduction using co-deposition techniques. The evolution of the proton involved a mechanism of the electrochemical reduction of both GO and AuNPs in acidic medium. The heterogeneous electron-transfer properties of this multilayer film were evaluated. The reductions *via* the electrochemical codeposition minimized the topological defects of rGO. This work provided a potential candidate for label-free DNA sensing with a lower LOD of 3.64×10^{-14} M, higher selectivity and sensitivity and lower hybridization efficiency resulting from the large number of ssDNA immobilized on the electrode interface. Computational description of the system through DFT calculations suggested that the most probable site for coordination of a gold nanocluster to rGO were the epoxy functional groups located on the graphene surface, rather than the carboxyl or hydroxyl groups. The coordination of the metal allowed the healing of the structural defects of graphene, and thus improved the conductivity and stability of the system.

4. Experimental

4.1. Chemicals

Gold wire (1.6 mm diameter) with a purity of 99.99% was obtained from CH Instruments, USA. Thiolated short-chain 27-mer synthetic oligonucleotides with HPLC-purified sequences of food pathogen DNA were obtained from MWG Biotech, Ebersberg, Germany. Their base sequences were as follows: 5-HS-(CH2)6-AAATGAACGCCCCAAAGGATTTACATTTTC-3 (I) (used as the capture ssDNA), 5-GAAAATGTAAATCCTTTGGGG-CGTTCATTT-3 (II) (used as the complementary target ssDNA (cDNA)), 5-TGTACCAGACGATGTGTACCAATGAGC GTG-3 (used as the non-complementary ssDNA (ncDNA)) and 5GAAAATGT-AAATCATTTGGGGCG TTCATTT-3 (IV) (used as the single base mismatch ssDNA (smDNA)). Graphite powders were purchased from Loba Chemie Pvt. Ltd, Mumbai, India. GO was synthesized from graphite in combination with Hummer's method (see the synthesis of GO in the ESI†), and its morphology was characterized by both SEM and TEM (Fig. S9†). The other chemicals, such as H_2SO_4, $HAuCl_4{\cdot}3H_2O$ and $K_3[Fe(CN)_6]$, were obtained from Sigma-Aldrich (St Louis, MO, USA). Double distilled water was used to prepare all the solutions.

4.2. Measurements and instrumentation

CV and EIS measurements were performed using an electrochemical instrument (model 650D, 440B, CH Instruments Inc., USA). SEM images were obtained using an Hitachi-S-4300 (Germany). AFM images were obtained using the APE Research model no: A100SGS instrument with tapping mode. Attenuated total reflection-FTIR (ATR-FTIR) spectra were recorded using a PerkinElmer Nicolet ISI in the frequency range from 4000 to 400 cm^{-1}. XPS analysis was carried out

using a Kratos-Axis Ultra instrument with a hemispherical 165 nm electron energy analyser. A BRUKER RES 27 MODEL was used for the Raman analysis, and spectra were recorded in the frequency range from 4000 to 50 cm^{-1} with a laser source of neodymium (Nd):YAG at 1064 nm. XRD (X'Pert PRO PANalytical) analysis was performed with Cu-Kα radiation as a source and an applied potential of 20 kV in the range from 10° to 80° with 1 s per step. SERS measurements were made using a confocal Raman microscope (CRM) 200; CRM-Alpha-300s, WITec, GmbH, Germany with an Ar ion laser (514.5 nm), and the spectral range was from 10× to 100× with a scan range of 100 × 100 micrometres. Electrochemical experiments were performed using a three-electrode system comprising a gold working electrode, a platinum wire counter electrode and a Ag/AgCl reference electrode. All the impedance data were obtained by Nyquist plots and fitted using Randle's equivalent circuit,[19] where R_s is the solution resistance, R_{ct} is the charge transfer resistance, CPE is the constant phase element and W is the Warburg impedance.

4.3. Construction of the 3D AuNPs/rGO/AuNPs/GCE

2 mg GO was dissolved in 1 ml double distilled water. A GO homogeneous suspension was obtained by ultrasonication for 2 h. Subsequently, the GO suspension was added into a mixture of $HAuCl_4$ solution containing H_2SO_4 (1 : 2 ratio of 2 mM $HAuCl_4{\cdot}3H_2O$ and 0.5 M H_2SO_4); then the mixed solution was ultrasonicated for 45 min. The 3D LBL AuNPs/rGO/AuNPs/GCE was obtained by CV in H_2SO_4 solution (0.1 M, pH = 1). The applied potential range was −0.25 to 0.4 V with a scan rate of 50 mV s^{-1} to ensure the simultaneous reduction of both GO and $HAuCl_4$ on the GCE surface.

4.4. Computational details

The nanoarchitecture of the AuNPs/rGO/AuNPs was confirmed by theoretical approximations. Because of the size of the system, the rGO layer was represented by a 16 × 16 $Å^2$ structure, which was in accordance with the experimental results. The AuNPs were represented by a two atoms cluster (Au_2). The geometry of rGO was fully optimized at the density functional theory (DFT) level using the Gaussian 09 computational package.[41] With the aim of studying the most stable site of coordination between the AuNPs and rGO, full geometry optimization of the complexation reactions between rGO and Au_2 was performed using the Becke's three-parameter nonlocal hybrid exchange potential with the nonlocal correlation functional of Lee, Yang, and Parr (B3LYP)[42–44] without any symmetry restriction. The triple-ζ 6-31G basis set was set for light atoms (C, H, O, N) along with a relativistic effective core potential basis set with pseudopotentials for gold atoms: LANL2DZ.[45] A tight SCF convergence criterion (10^{-8} a.u.) was used in all the calculations. As implemented in Gaussian09, the charge distribution of intermolecular interactions was calculated using the natural population analysis (NPA) method.[46] The interaction energy (E_{int}) was defined as the energy difference between the complex and the energies of the constituent monomers and was calculated using eqn (5).† The computation of this quantity with finite basis sets introduces an error known as the basis set superposition error (BSSE) because different numbers of basic functions were used to describe the complex and monomers for the same basis set. BSSE-corrected interaction energies were computed using the Boys–Bernardi counterpoise correction scheme.[47] The effect on the conductivity of the coordination of gold to graphene was estimated for rGO and for defective reduced graphene oxide (rGOd), which was built on the basis of a previous study reported by Lim and coworkers.[48] The conductivity was related to the theoretical energy band gap (E_{bg}), which corresponded to the energy difference between respective eigenvalues of frontier molecular orbitals HOMO and LUMO, as follows: $E_{bg} = (E_{LUMO} - E_{HOMO})$ eV.

4.5. Immobilization and hybridization of DNA

Thiolated DNA was easily immobilized onto the surface of the 3D LBL AuNPs/rGO/AuNPs/GCE by gold–thiol interactions (Scheme 1). Namely, 7 μM thiolated DNA containing 1 M NaCl solution was dropped on the surface of the 3D LBL AuNPs/rGO/AuNPs/GCE. The self-assembly of the functionalized DNA containing thiol groups onto the surface of the 3D LBL AuNPs/rGO/AuNPs/GCE was generally formed. After 2 h, probe I (DNA bioelectrode) was rinsed using phosphate buffer solution (PBS, pH = 7.4) to remove the non-immobilized DNA. Then, probe I was used to hybridize with 7 μl of 1 μM of cDNA, ncDNA or smDNA buffer for 2 h, respectively. Finally, the as-obtained different probes were rinsed several times with 10 mM PBS (pH 7.4) to remove the non-hybridized DNA *via* physical absorption.

Conflicts of interest

The authors declare no competing financial interests.

Acknowledgements

The work financially supported by the CSIR No. 03(1160)/10/EMR-II, DST-INSPIRE Grant (DST/INSPIRE/04/2015/000337), Fondecyt Chile (11140107), and NSFC (51662014).

Notes and references

1 A. Bonanni and M. Del-Valle, *Anal. Chim. Acta*, 2010, **678**, 7–17.
2 L. Wu, E. Xiong, X. Zhang, X. H. Zhang and J. H. Chen, *Nano Today*, 2014, **9**, 197–211.
3 F. Lucarelli, G. Marrazza, A. P. F. Turner and M. Mascini, *Biosens. Bioelectron.*, 2004, **19**, 515–530.
4 H. F. Teh, H. Q. Gong, X. D. Dong, X. T. Zeng, A. L. K. Tan, X. H. Yang and S. N. Tan, *Anal. Chim. Acta*, 2005, **551**, 23–29.
5 R. L. McCreery, *Chem. Rev.*, 2008, **108**, 2646–2687.
6 D. W. Wang and D. Su, *Energy Environ. Sci.*, 2014, **7**, 576–591.

7 W. Zhang, S. Zhu, R. Luque, S. Han, L. Hu and G. Xu, *Chem. Soc. Rev.*, 2016, **45**(3), 715–752.
8 C. Yang, M. E. Denno, P. Pyakurel and B. J. Venton, *Anal. Chim. Acta*, 2015, **887**, 17–37.
9 J. N. Tiwari, V. Vij, K. C. Kemp and K. S. Kim, *ACS Nano*, 2016, **10**, 46–80.
10 T. Yoon, J. H. Kim, J. H. Choi, D. Y. Jung, I. J. Park, S. Y. Choi, N. S. Cho, J. I. Lee, Y. D. Kwon, S. Cho and T. S. Kim, *ACS Nano*, 2016, **10**, 1539–1545.
11 D. Y. Kim, S. Sinha-Ray, J. J. Park, J. G. Lee, Y. H. Cha, S. H. Bae, J. H. Ahn, Y. C. Jung, S. M. Kim, A. L. Yarin and S. S. Yoon, *Adv. Funct. Mater.*, 2014, **24**, 4986–4995.
12 O. K. Park, Y. M. Choi, J. Y. Hwang, C. M. Yang, W. T. Kim, N. H. You, H. Y. Koo, J. H. Lee, B. C. Ku and M. Goh, *Nanotechnology*, 2013, **24**, 185604.
13 E. D'Elia, S. Barg, N. Ni, V. G. Rocha and E. Saiz, *Adv. Mater.*, 2015, **27**, 4788–4794.
14 X. Liu, F. Wang, W. Wang and H. Wu, *Carbon*, 2016, **107**, 680–688.
15 H. Cai, C. Xu, P. He and Y. Fang, *J. Electroanal. Chem.*, 2001, **510**, 78–85.
16 H. Ma. L. Zhang, Y. Pan, K. Zhang and Y. Zhang, *Electroanalysis*, 2008, **20**, 1220–1226.
17 K. Turcheniuk, R. Boukherroub and S. Szunerits, *J. Mater. Chem. B*, 2015, **3**, 4301–4324.
18 K. Jayakumar, R. Rajesh, V. Dharuman, R. Venkatasan, J. Hahn and S. K. Pandian, *Biosens. Bioelectron.*, 2012, **31**, 406–412.
19 P. A. Rasheed, T. Radhakrishnan, P. K. Shihabudeen and N. Sandhyarani, *Biosens. Bioelectron.*, 2016, **83**, 361–367.
20 H. Cai, C. Xu, P. He and Y. Fang, *J. Electroanal. Chem.*, 2001, **510**, 78–85.
21 K. Hu, D. Lan, X. Li and S. Zhang, *Anal. Chem.*, 2008, **80**, 9124–9130.
22 C. Xue, M. Gao, Y. Xue, L. Zhu, L. Dai, A. Urbas and Q. Li, *J. Phys. Chem. C*, 2014, **118**, 15332–15338.
23 C. Xue, C. C. Kung, M. Gao, C. C. Liu, L. Dai, A. Urbas and Q. Li, *Sens. Biosensing Res.*, 2015, **3**, 7–11.
24 M. Keeney, X. Y. Jiang, M. Yamane, M. Lee, S. Goodman and F. Yang, *J. Mater. Chem. B*, 2015, **3**, 8757–8770.
25 S. Y. Toh, K. S. Loh, S. K. Kamarudin and W. R. W. Daud, *Chem. Eng. J.*, 2014, **251**, 422–434.
26 D. Bom, R. Andrews, D. Jacques, J. Anthony, B. Chen, M. S. Meier and J. P. Selegue, *Nano Lett.*, 2002, **2**, 615–619.
27 K. N. Kudin, B. Ozbas, H. C. Schniepp, R. K. P. homme, I. A. Aksay and R. Car, *Nano Lett.*, 2008, **8**(1), 36–41.
28 A. Benvidi, A. Dehghani-Firouzabadi, M. Mazloum-Ardakani, B. B. F. Mirjalili and R. Zare, *J. Electroanal. Chem.*, 2015, **7**, 22–36.
29 P. Zhang, Y. Huang, X. Lu, S. Zhang, J. Li, G. Wei and Z. Su, *Langmuir*, 2014, **30**, 8980–8989.
30 M. A. Raj and S. A. John, *J. Phys. Chem. C*, 2013, **117**, 4326–4335.
31 X. Zhao, P. Zhang, Y. Chen, Z. Su and G. Wei, *Nanoscale*, 2015, **7**, 5080–5093.
32 A. J. Bandodkar, C. S. Lopez, A. M. V. Mohan, L. Yin, R. Kumar and J. Wang, *Sci. Adv.*, 2016, **2**, 1–10.
33 J. J. Richardson, J. Cui, M. Bjornmalm, J. A. Braunger, H. Ejima and F. Caruso, *Chem. Rev.*, 2016, **116**, 14828–14867.
34 R. Rozada, J. I. Paredes, M. J. Lopez, S. Villar-Rodil, I. Cabria, J. A. Alonso, A. Martinez-Alonso and J. M. D. Tascon, *Nanoscale*, 2015, **7**, 2374–2390.
35 C. Punckt, M. A. Pope, Y. M. Liu and I. A. Aksay, *J. Electrochem. Soc.*, 2016, **163**, H491–H498.
36 I. Khalil, N. M. Julkapli, W. A. Yehye, W. J. Basirun and S. K. Bhargava, *Materials*, 2016, **9**(6), 406–444.
37 C. Gomez-Navarro, J. C. Meyer, R. S. Sundaram, A. Chuvilin, S. Kurasch, M. Burghard, K. Kern and U. Kaiser, *Nano Lett.*, 2010, **10**(4), 1144–1148.
38 R. S. Nicholson, *Anal. Chem.*, 1965, **37**(11), 1351–1355.
39 A. Ambrosi, C. K. Chua, N. M. Latiff, A. H. Loo, H. A. Wong, A. Yong and M. Pumera, *Chem. Soc. Rev.*, 2016, **45**, 2458–2493.
40 Y. Hu, F. Li, D. Han, T. Wu, Q. Zhang, L. Niu and Y. Bao, *Anal. Chim. Acta*, 2012, **753**, 82–89.
41 M. J. Frisch, G. W. Trucks, H. B. Schlegel, G. E. Scuseria, M. A. Robb, J. R. Cheeseman, G. Scalmani, V. Barone, B. Mennucci, G. A. Petersson, H. Nakatsuji, M. Caricato, X. Li, H. P. Hratchian, A. F. Izmaylov, J. Bloino, G. Zheng, J. L. Sonnenberg, M. Hada, M. Ehara, K. Toyota, R. Fukuda, J. Hasegawa, M. Ishida, T. Nakajima, Y. Honda, O. Kitao, H. Nakai, T. Vreven, J. A. Montgomery, J. E. Peralta, M. Ogliaro, M. Bearpark, J. J. Heyd, E. Brothers, K. N. Kudin, V. N. Staroverov, R. Kobayashi, J. Normand, K. Raghavachari, A. Rendell, J. C. Burant, S. S. Iyengar, J. Tomasi, M. Cossi, N. Rega, J. M. Millam, M. Klene, J. E. Knox, J. B. Cross, V. Bakken, C. Adamo, J. Jaramillo, R. Gomperts, R. E. Stratmann, O. Yazyev, A. J. Austin, R. Cammi, C. Pomelli, J. W. Ochterski, R. L. Martin, K. Morokuma, V. G. Zakrzewski, G. A. Voth, P. Salvador, J. J. Dannenberg, S. Dapprich, A. D. Daniels, J. B. Farkas, J. B. Foresman, J. V. Ortiz, J. Cioslowski and D. J. Fox, *Revision A.01, Gaussian*, 2009.
42 A. D. Becke, *J. Chem. Phys.*, 1993, **98**, 5648–5652.
43 C. Lee, W. Yang and R. G. Parr, *Phys. Rev. B: Condens. Matter Mater. Phys.*, 1988, **37**, 785–789.
44 P. J. Stephens, F. J. Devlin, C. F. Chabalowski and M. Frisch, *J. Phys. Chem.*, 1994, **98**(45), 11623–11627.
45 P. J. Hay and W. R. Wadt, *J. Chem. Phys.*, 1985, **82**(1), 270–283.
46 A. E. Reed, R. B. Weinstock and F. Weinhold, *J. Chem. Phys.*, 1985, **83**, 735–746.
47 S. F. Boys and F. Bernardi, *Mol. Phys.*, 1970, **19**, 553–566.
48 D. H. Lim, A. S. Negreira and J. Wilcox, *J. Phys. Chem. C*, 2011, **115**, 8961–8970; *Essentials of Glycobiology*, ed. A. Varki, R. D. Cummings, J. D. Esko, H. H. Freeze, P. Stanley, C. R. Bertozzi, G. W. Hart and M. E. Etzler, Cold Spring Harbor Laboratory Press, Cold Spring Harbor, NY, 2nd edn, 2009.

